vehicles

MDPI

Article

Early Driver Fatigue Detection System: A Cost-Effective and Wearable Approach Utilizing Embedded Machine Learning

Chengyou Lin [1], Xinying Zhu [2], Renpeng Wang [2], Wei Zhou [2], Na Li [1,*] and Yu Xie [2,*]

[1] Public Security Department, Fujian Police College, Fuzhou 350007, China
[2] Pen-Tung Sah Institute of Micro-Nano Science and Technology, Xiamen University, Xiamen 361102, China; weizhou@xmu.edu.cn (W.Z.)
* Correspondence: linaapp@163.com (N.L.); xieyu@xmu.edu.cn (Y.X.)

Abstract: Driving fatigue is the cause of many traffic accidents and poses a serious threat to road safety. To address this issue, this paper aims to develop a system for the early detection of driver fatigue. The system leverages heart rate variability (HRV) features and embedded machine learning to estimate the driver's fatigue level. The driver's HRV is derived from electrocardiogram (ECG) signals captured by a wearable device for analysis. Time- and frequency-domain HRV features are then extracted and used as the input for a machine learning classifier. A dataset of HRV features is collected from a driving simulation experiment involving 18 participants. Four machine learning classifiers are evaluated, and a backpropagation neural network (BPNN) is selected for its superior performance, achieving up to 94.35% accuracy. The optimized classifier is successfully deployed on an embedded system, providing a cost-effective and portable solution for the early detection of driver fatigue. The results demonstrate the feasibility of using HRV-based machine learning models for the early detection of driver fatigue, contributing to enhanced road safety and a reduced accident risk.

Keywords: fatigue driving detection; heart rate variability; embedded machine learning; electrocardiogram; wearable device; embedded system

check for updates

Academic Editor: Franck Mars

Received: 16 November 2024
Revised: 27 December 2024
Accepted: 6 January 2025
Published: 8 January 2025

Citation: Lin, C.; Zhu, X.; Wang, R.; Zhou, W.; Li, N.; Xie, Y. Early Driver Fatigue Detection System: A Cost-Effective and Wearable Approach Utilizing Embedded Machine Learning. *Vehicles* **2025**, *7*, 3. https://doi.org/10.3390/vehicles7010003

Copyright: © 2025 by the authors. Licensee MDPI, Basel, Switzerland. This article is an open access article distributed under the terms and conditions of the Creative Commons Attribution (CC BY) license (https://creativecommons.org/licenses/by/4.0/).

1. Introduction

Fatigue driving is one of the major causes of traffic accidents worldwide, contributing to approximately 18% of all traffic-related fatalities between 2017 and 2021, totaling nearly 30,000 deaths, according to the AAA Foundation for Traffic Safety [1]. This issue not only endangers drivers' lives but also imposes significant social and economic costs, such as increased healthcare expenditures and insurance claims. As traffic safety remains a critical public health priority, fatigue-related accidents have become an urgent concern for authorities globally. To reduce the risk of fatigue driving, policies have begun to be implemented around the world which focus on the management of drivers' working hours and restrict long-term driving [2–4]. However, these measures largely rely on drivers' self-discipline or enforcement by authorities, which cannot impose driving restrictions during the early stages of fatigue.

This is concerning because early intervention is crucial, as fatigue at its early stages can already begin to impair drivers' reaction times and decision-making. This limitation highlights the need for more reliable and proactive approaches to fatigue detection that can provide real-time monitoring and intervention.

The existing proactive fatigue detection methods are mainly based on behavioral characteristics, vehicle travel data, and physiological signals [5–7], with recent methods

also integrating multimodal information for improved detection [8–13]. Behavioral signal detection mainly identifies fatigue status by monitoring behavioral characteristics such as the driver's facial expressions, eye movements, head posture, yawning [14–19], etc. These methods typically rely on machine learning approaches to extract and analyze complex behavioral patterns, enabling a more precise detection of fatigue. However, environmental factors such as the lighting conditions and obstructions caused by accessories like glasses can significantly reduce their accuracy, leading to inconsistent detection results and limited practical applications [5,6,18,19]. Additionally, even with advancements in model compression and distillation techniques that allow for the creation of compact, high-accuracy models, deploying these models on resource-constrained devices remains a significant challenge [7]. Vehicle travel data detection infers the driver's status by analyzing vehicle operation data such as the vehicle's speed, acceleration, steering wheel angle, lane deviation [20,21], etc. However, the effectiveness of vehicle driving data detection is heavily influenced by external factors such as road conditions and individual driving habits, which can make it difficult to achieve consistent results. Furthermore, these methods lack the capability for early detection, reducing their utility in providing timely warnings of driver fatigue.

On the other hand, physiological signal-based detection methods have emerged as an effective alternative. Physiological signal-based detection methods recognize fatigue by monitoring changes in bioelectric signals such as those obtained from electroencephalograms (EEGs) [22–27], electrocardiograms (ECGs) [28–31], electrooculograms (EOGs) [32–35], and electromyograms [36]. These methods provide accurate and reliable fatigue assessment by directly capturing the body's physiological responses [37,38]. Among these, the ECG-derived heart rate variability (HRV) is an effective indicator for detecting fatigue due to its non-invasive nature and strong correlation with the autonomic nervous system (ANS) [39]. The effectiveness of HRV as a fatigue detection indicator has been further confirmed in experiments in naturalistic driving scenarios [40]. The authors found that the HRV indicators of 24 professional truck drivers with different truck configurations changed consistently over extended periods of driving and aligned with their subjective reports of the task demand, validating that HRV is a reproducible and precise indicator of fatigue under real-world driving conditions. Additionally, HRV has been recognized as an early indicator of fatigue, making it ideal for use as an early warning sign in dynamic driving conditions [40,41].

At the same time, the increasing availability of wearable devices with ECG capabilities has opened up new possibilities for real-time HRV-based fatigue detection. However, the current commercially available ECG wearable devices are mostly used for heart health monitoring and are not specifically designed for driving fatigue detection. For example, devices such as WHOOP (WHOOP Inc., Boston, MA, USA) [42] and Oura Ring (Oura Health Ltd., Oulu, Finland) [43] are mainly used to monitor HRV to assess health status and recovery. Some motion-oriented devices with HRV detection, such as Garmin (Garmin Ltd., Olathe, KS, USA) [44], Fitbit (Fitbit Inc., San Francisco, CA, USA) [45], and Apple Watch (Apple Inc., Cupertino, CA, USA) [46], have high monitoring accuracy, but still have deficiencies regarding their use in fatigue detection algorithms and their adaptation to driving scenarios. In addition, the high cost of these devices limits their widespread use in single-purpose applications such as fatigue detection. These limitations suggest the current gap between the commercially available wearable devices and the practical needs of driver fatigue detection systems. Therefore, the motivation of this work is to develop an affordable and efficient wearable system for early fatigue detection, addressing the limitations of current ECG-based devices and meeting the urgent need for proactive solutions to prevent fatigue-related accidents. Leveraging recent advances in embedded machine learning

technology offers a promising direction to achieve this [47,48]. Embedded machine learning enables fatigue detection systems to achieve low latency, low power consumption, and high privacy by processing data directly on the embedded device [19,49–51]. As traditional machine learning models are more computationally efficient and better suited for use in embedded devices with limited resources compared to deep learning, this study is dedicated to exploring a low-cost integration of embedded machine learning algorithms with hardware platforms.

Based on these motivations, this paper proposes an early fatigue detection scheme based on an embedded system to address the challenges of existing fatigue detection approaches. Through a driving simulation experiment, this study collected HRV data from 18 participants and constructed a physiological signal dataset for training machine learning models to detect driving fatigue. To meet accuracy requirements, this paper evaluated four machine learning algorithms and finally selected a lightweight backpropagation neural network (BPNN) and optimized its structure to adapt to resource-constrained embedded devices. The model achieved a detection accuracy of 94.35% in the simulation experiment. In addition, this paper also analyzed the changing trends of HRV features before and after the fatigue state and their gender differences. The main contributions of this paper are as follows:

- Early Detection of Driver Fatigue: By leveraging HRV features extracted from ECG signals, this study presents an innovative framework for the early detection of fatigue. Unlike the existing systems that often detect fatigue at advanced stages, our approach emphasizes proactive intervention by identifying physiological changes in the early stages of fatigue with reliable accuracy, improving driver safety;
- Investigation of Gender Differences: This study pioneers the exploration of gender-specific variations in HRV features during fatigue states. By investigating the impact of gender on drivers' physiological responses, our work lays the foundation for developing tailored, gender-sensitive fatigue detection models that enhance accuracy and inclusivity in real-world applications;
- Low-Cost, Wearable Solution: The proposed system leverages embedded machine learning algorithms to deliver a significantly lower cost and higher portability compared to existing vehicle-integrated driver fatigue detection systems, providing an affordable and practical wearable solution for diverse vehicles and drivers;

The remainder of this paper is organized as follows: Section 2 provides a comprehensive overview of the system architecture and methodologies used, including the embedded system architecture, data processing techniques, simulated driving experiment setup, and machine learning algorithms. Section 3 presents the experimental results, including an analysis of the HRV dataset and performance comparisons of different machine learning models. Section 4 provides an in-depth discussion of the results, and Section 5 concludes this paper and suggests potential directions for future research.

2. Materials and Methods

2.1. System Overview

The fatigue driving detection system in this paper uses the STM32F407ZGT6 microcontroller unit (MCU) from STMicroelectronics (Geneva, Switzerland) as the main control unit. This MCU is based on a high-performance Cortex-M4 core (ARM Ltd., Cambridge, UK) and integrates a single-precision floating-point unit (FPU) and a digital signal processing (DSP) unit. It supports all ARM single-precision data-processing instructions and data types, allowing full DSP instruction execution, which meets the requirements of this embedded system for HRV analysis in both time and frequency domains.

The overall system architecture is shown in Figure 1. The system first uses the AD8232 module to capture ECG signals, which are then preprocessed by the STM32F407ZGT6 MCU for HRV feature extraction. The MCU uses an analog-to-digital converter (ADC) and timers for signal acquisition, as well as utilizing direct memory access (DMA)

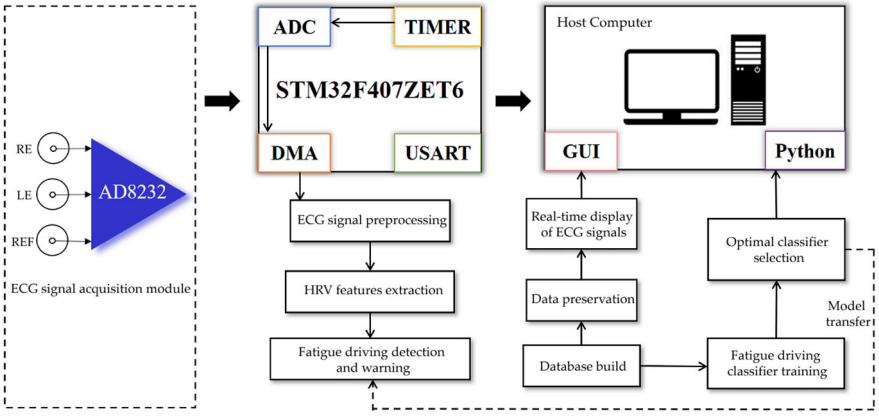


Figure 1. The architecture of the fatigue detection system. RE, LE, and REF represent the Right Electrode, Left Electrode, and Reference Electrode, respectively.

DMA is used for data transfer and communicates with the host computer through a USART interface. The host computer displays real-time ECG signals and stores data via a graphical user interface (GUI), while Python (version 3.8.5) is used for classifier model training and optimization. Finally, the optimized classifier model is deployed to the MCU for fatigue driving warnings.

2.2. ECG Data Acquisition

2.2.1. Electrodes Placement

After processing with a gain of 400 times, the AD8232 chip outputs the signal to the PA5 pin of the MCU, ensuring that the signal amplitude is within the range of 0–1.6 V for easy acquisition and processing by the MCU's analog-to-digital converter. To ensure the portability of the detection device, this paper adopts a single-lead ECG recording. Two electrodes are placed on the driver's skin surface to measure the potential difference between their arms, with a third electrode serving as a reference. The electrodes are of the disposable Ag-AgCl type, with a non-woven fabric adhesive surface, and solid conductive gel is used to ensure firm attachment to the skin surface.

As shown in Figure 2, the AD8232 ECG acquisition module provides two electrode placement schemes: in Scheme 1, the electrodes are placed on the chest near the heart, and in Scheme 2, the electrodes are placed on the wrists and thighs. By comparing the signal outputs of the two electrode placement schemes, it is found that Scheme 1 has a larger signal amplitude and less noise because it is close to the heart and less affected by motion, while Scheme 2 has electrodes placed on the wrists and legs, which are easily affected by hand movements during driving, resulting in the signal quality being poor. Therefore, Scheme 1 is more suitable for fatigue detection in actual driving.

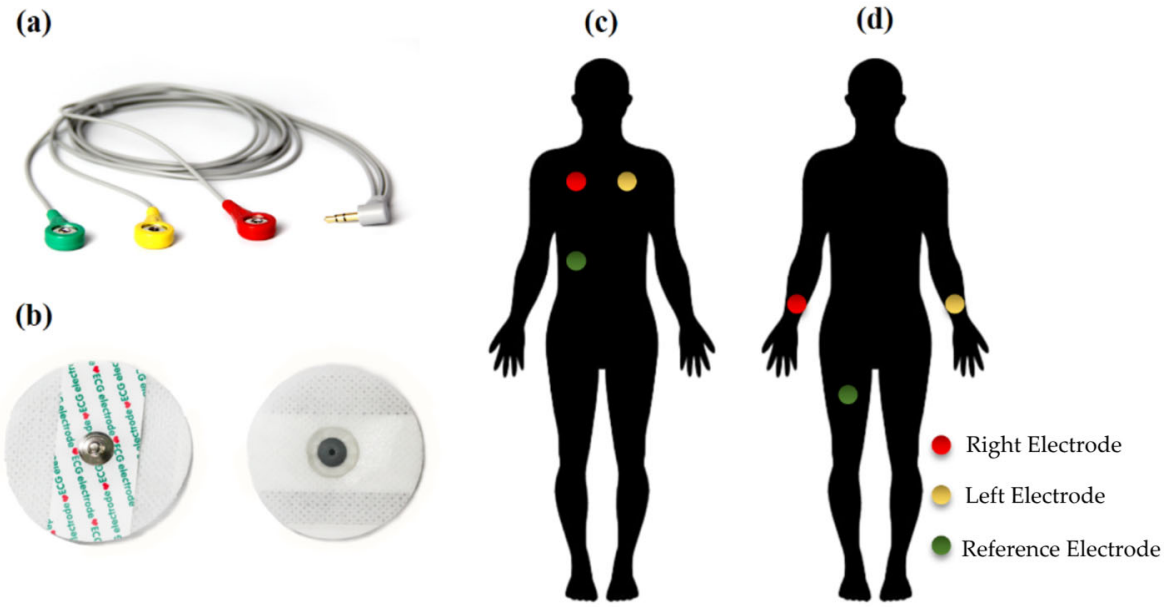


Figure 2. Electrode placement and ECG acquisition setup. (**a**) ECG electrode connection cables; (**b**) Ag-AgCl disposable electrodes; (**c**) electrode placement Scheme 1 (chest); (**d**) electrode placement Scheme 2 (wrist and thigh).

2.2.2. Data Sampling and Transmission

The ECG signal is converted through the MCU's 12-bit ADC unit. By configuring the ADC-CCR register, the ADC is set to independent mode, with a prescaler coefficient (PSC) of 4 and a sampling phase delay of 5 cycles. During ADC initialization, a single conversion mode is used, triggered by the rising edge of the timer, with the right alignment enabled. Studies have shown that nearly 99% of the spectral energy of the QRS wave in ECG signals is concentrated within the 0–40 Hz range [52]. Therefore, the sampling frequency f_s is set to 200 Hz in this system, with the timer-triggered sampling frequency calculated as follows:

$$T_{out} = \frac{(ARR + 1)(PSC + 1)}{T_{CLK}}. \quad (1)$$

The PSC is set to 167, the auto-reload value ARR is 4999, and the timer input clock frequency T_{CLK} is 168 MHz, resulting in T_{out} = 0.005 s (i.e., a frequency of 200 Hz).

Subsequently, the system uses DMA for data transfer, employing a cyclic acquisition mode to ensure continuity for long-term data collection. DMA and interrupt mechanisms are enabled, and when ECG signal acquisition is complete, the interrupt flag changes from 0 to 1. The main program checks the flag status, and if it is 1, it proceeds with ECG signal preprocessing, R-wave detection, HRV time–frequency analysis, and feature extraction. If the flag is 0, it continues to wait for data acquisition to be complete (as shown in Figure 3). Finally, since the model needs to be trained on the host computer, the ECG data are transmitted in real time from the STM32 microcontroller to the host computer via a serial port. The collected data are stored and processed on the host computer, where HRV features are extracted and input into the Python environment for training and testing machine learning models.

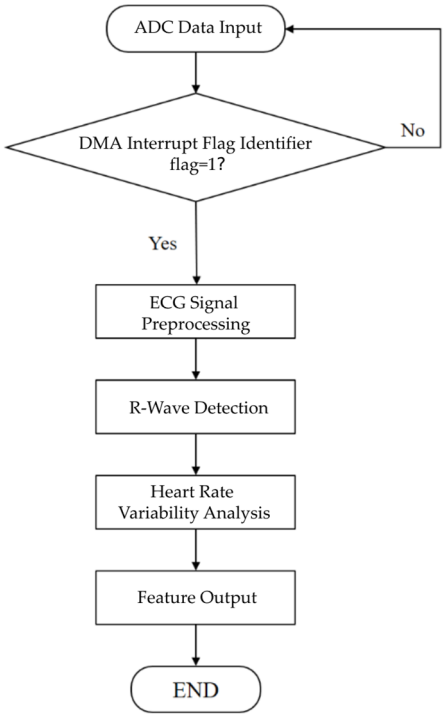


Figure 3. Flowchart of ECG data acquisition and processing.

2.3. ECG Signal Processing and Feature Extraction

2.3.1. Noise Filtering

Common sources of noise in ECG signals include powerline interference, baseline wander, and electromyography (EMG) noise. Therefore, effective signal preprocessing methods are needed to eliminate these noises. Powerline interference consists of a 50 Hz sinusoidal signal and its harmonics, while EMG noise is high-frequency noise above 100 Hz [53]. Therefore, this paper employs a Butterworth low-pass filter to perform preliminary filtering on the collected ECG signals. The design of the Butterworth filter first defines its ideal frequency response in the analog domain:

$$|H(j\omega)|^2 = \frac{1}{1 + \left(\frac{\omega}{\omega_c}\right)^{2N}}, \tag{2}$$

where ω_c is the cutoff frequency and N is the filter order. The discrete implementation is achieved through the following difference equation:

$$y(n) = -\sum_{i=0}^{N} a_i y(n-i) + \sum_{i=1}^{M} b_i x(n-i), \tag{3}$$

where $x(n)$ is the input sequence, $y(n)$ is the output sequence, a_i and b_i are the filter coefficients, and M and N are the orders of the input and output signals, respectively. Applying the Z-transform to this equation yields the Z-domain transfer function

$$H(z) = \frac{Y(z)}{X(z)} = \frac{\sum_{i=0}^{M} b_i z^{-i}}{1 + \sum_{i=1}^{N} a_i z^{-i}}. \tag{4}$$

By using the FDATool in MATLAB (version R2019b), and setting the filter order to 4, sampling frequency to 200 Hz, and cutoff frequency to 50 Hz, we obtained the corresponding filter coefficients a_1, a_2, b_0, b_0, and b_2. These coefficients were imported into the MCU, and low-pass filter code was written using ARM's DSP library. This library

implements low-pass filtering based on a second-order Biquad cascade structure, where each Biquad is a second-order filter described by the difference equation

$$y[n] = b_0 \cdot x[n] + b_1 \cdot x[n-1] + b_2 \cdot x[n-2] + a_1 \cdot y[n-1] + a_2 \cdot y[n-2]. \quad (5)$$

To eliminate baseline wander, this paper uses a zero-phase filtering method. This approach applies forward and reverse filtering to achieve the accurate filtering of ECG signals, avoiding the interference of baseline wander on the ST-T segment of the ECG signal. For this purpose, a second-order Butterworth low-pass filter was designed with a cutoff frequency of

$$f_c = \frac{f_{max}}{f_s/2}, \quad (6)$$

where f_{max} is 5 Hz, and the filter coefficients are generated and exported through FDATool. The filtering process consists of four steps: first, ECG data are read and extended at the end; then, the data are input into the filter for forward filtering; next, the signal is time-reversed, and reverse filtering is applied; finally, the output result is reversed, the extended data are removed, and the filtered signal is output.

2.3.2. R-Wave Detection

To accurately detect R-waves, the Pan–Tompkins algorithm [54] was implemented in MATLAB during the data processing stage. This algorithm utilizes adaptive thresholding to track signal changes, which improves the accuracy of R-wave detection.

Due to the resource constraints of the MCU, a simplified detection method was applied for the embedded implementation. In this approach, the ECG signal is processed with a point-difference operation to highlight peak features, calculated as

$$diff[i] = x[i+1] - x[i-1]. \quad (7)$$

Based on this difference signal, a signal threshold (set to 0.8 times the maximum) is applied to filter potential R-wave peaks. If the difference changes from positive to negative, a candidate peak is identified, and it is confirmed as an R-wave if it exceeds the signal threshold. The interval between successive R-waves is then calculated for HRV analysis, with intervals below 400 ms excluded to remove artifacts.

2.3.3. HRV Feature Extraction

Heart rate variability (HRV) analysis constructs an RR interval sequence by calculating the time difference between consecutive R-waves for time-domain and frequency-domain analysis, extracting features of the ECG signal. The calculation formula is

$$RR_i = R_{i+1} - R_i, \quad (8)$$

where RR is the time series of RR intervals, representing the HRV signal, R_{i+1} is the time of the next R-wave, and R_i is the time of the current R-wave.

Time-domain analysis is based on statistical metrics of the RR interval sequence. Specific features, formulas, and their physiological interpretations [41] are detailed in Table 1. Frequency-domain analysis uses the fast Fourier transform (FFT) and Welch methods [55] to analyze the power distribution across different frequency bands. Notably, to meet FFT requirements, the RR interval sequence was interpolated to 1024 points using cubic spline interpolation; specific frequency-domain features are provided in Table 2.

Table 1. Time-domain analysis features for HRV.

Features Name	Description	Calculation Formula	Unit	Physiological Interpretation
AVNN	Mean RR interval	$\frac{(\sum_{i=0}^{N} RR_i)}{N}$	ms	Basic heart rhythm regulation
SDNN	Standard deviation of RR intervals	$sqrt(\frac{\sum_{i=0}^{N}(RR_i - AVNN)^2}{N-1})$	ms	Sympathetic and parasympathetic influence
RMSSD	Root mean square of successive differences of RR intervals	$sqrt(mean((RR_{i+1} - RR_i)^2))$	ms	Parasympathetic activity
pNN50	Percentage of adjacent RR intervals with difference >50 m	$\frac{count(\lvert RR_{i+1} - RR_i \rvert)_{>50ms}}{N-1} \times 100\%$		Parasympathetic regulation
HR	Average heart rate	$\frac{60}{AVNN}$	bpm	Vagal activity

Table 2. Frequency-domain analysis features for HRV.

Features Name	Description	Calculation Formula	Unit	Physiological Interpretation
LF	Low-frequency power	0.04–0.15 Hz	s²/Hz	Sympathetic and parasympathetic activity
HF	High-frequency power	0.15–0.4 Hz	s²/Hz	Parasympathetic activity
LF/HF	Ratio of low to high-frequency power			Sympatho-vagal balance
LF (n.u.)	Normalized low frequency power	$LF(n.u.) = \frac{LF}{LF+HF} \times 100$	$n.u.$	Relative power of sympathetic activity
HF (n.u.)	Normalized high frequency power	$HF(n.u.) = \frac{HF}{LF+HF} \times 100$	$n.u.$	Relative power of parasympathetic (vagal) activity

2.4. Dataset Collection in Simulated Driving Experiment

2.4.1. Experiment Volunteers

This paper recruited 18 volunteers (9 male and 9 female), and their basic information is shown in Table 3. All volunteers had no history of cardiovascular disease, were in good health, and had no sleep disorders. Alcohol consumption was prohibited within 24 h before the experiment, and caffeinated beverages were not allowed within 12 h. The purpose of the experiment was explained to the volunteers in advance, and compensation was provided upon completion of the experiment.

Table 3. Basic information of experiment volunteers.

Attributes	Male (Mean ± SD)	Female (Mean ± SD)
age	23.1 ± 1.1 (year)	23.2 ± 1.2 (year)
height	177.0 ± 5.8 (cm)	165.1 ± 5.4 (cm)
weight	67.4 ± 10.3 (kg)	52.4 ± 4.8 (kg)

2.4.2. Simulated Driving Experiment Setup

To ensure the safety and controllability of the experiment, this paper adopted a simulated driving platform which consisted of two parts: an ECG signal acquisition device and a driving simulation system (as shown in Figure 4). The simulation used the "Euro Truck Simulator 2" software (version 1.52.0.3s), with hardware components like a steering wheel and pedals to mimic real-world driving conditions. The simulation setup

incorporated various scenarios to simulate stress, distraction, and dynamic environment changes, aiming to enhance participants' experience of driving fatigue:

- Stress simulation: to introduce stress, participants were given specific time-limited delivery tasks within the simulation. The tasks required maintaining a high level of concentration while adhering to strict schedules, replicating the time pressure often experienced in real-world driving. Additionally, penalties for errors, such as collisions or exceeding speed limits, were used to enhance stress levels;
- Distraction simulation: distraction was introduced by incorporating background auditory stimuli, such as random notifications and ambient noises, while participants navigated the simulated environment. These elements were designed to mimic real-life distractions, such as phone notifications or radio chatter, which can divert attention from driving;
- Dynamic environment changes simulation: the simulation included varying environmental conditions, such as sudden changes in weather (e.g., rain or fog), road types (e.g., highways vs. narrow streets), and traffic density. These scenarios replicated real-world driving challenges that require quick adaptation and heightened attention.

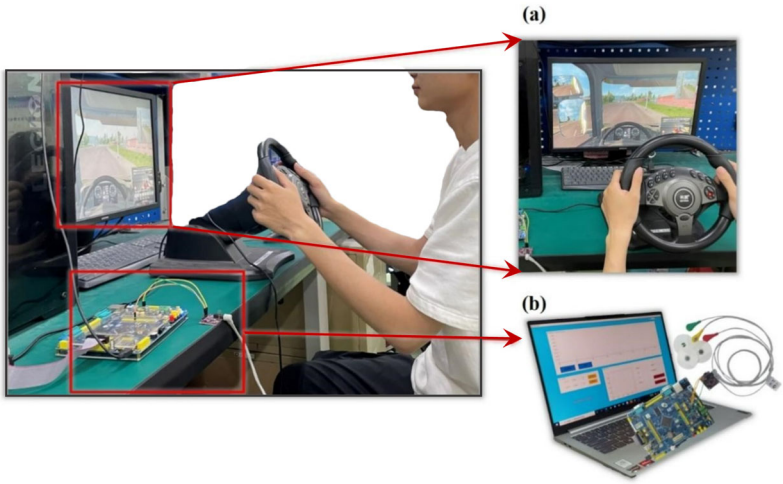


Figure 4. Simulated driving experiment platform. (**a**) Driving simulation system; (**b**) ECG signal acquisition device.

The ECG data acquisition device, previously introduced in Section 2.2, transmits ECG data to the host computer for processing and storage. To record the fatigue level shown by volunteers' EMG data during the experiment, this paper used the Karolinska Sleepiness Scale (KSS) [56] to score participants' subjective fatigue levels. Based on the scores, ECG signals were labeled as fatigue (1) or alert (0). Additionally, previous research has indicated that drivers' visual involuntary attention is related to their fatigue state [57]. Therefore, we also added a Go/No-Go visual involuntary attention experiment based on PEBL (Psychology Experiment Building Language, version 2.0) [58] (as shown in Figure 5) for volunteers. Participants were asked to press the left mouse button when the letter "P" appeared in one of the four cells, which might be initially covered by blue stars. No response was required if the letter "R" appeared. The KSS scores were then adjusted according to the match between the Go/No-Go experiment results (the ratio of accuracy to reaction time) and the subjective scores.

To ensure that fatigue levels were distinguishable across different experimental sessions, this paper divided the simulated driving experiment into three time periods: morning (10:00–11:00), afternoon (13:00–14:00), and evening (19:00–20:00), with each session lasting 1 h. Before the experiment, participants sat quietly and relaxed for 10 min. During the experiment, ECG signals were collected at 10 min intervals, with each collection lasting

5 min and a sampling rate of 200 Hz. Therefore, 6 HRV data samples were collected within each driving session. Each sample's interval was carefully designed to reflect the drivers' physiological states at different stages during the driving sessions. This design aims to avoid the issue of sample feature values being too similar due to short sampling intervals, ensuring that the model can learn generalized features that represent both alert and fatigued states. Furthermore, in practice, the feature values of the samples exhibit significant differences due to the dynamic changes in physiological states as well as the influence of distractions, stress, and other dynamic environmental factors. Before each signal collection, KSS subjective fatigue ratings and a visual involuntary attention test were conducted. The ambient temperature of the laboratory was maintained at 25 °C.

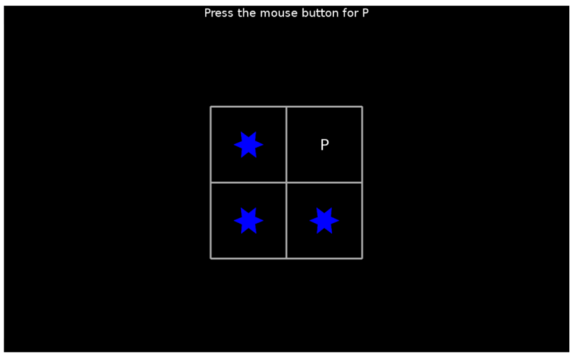


Figure 5. Visual involuntary attention experiment based on PEBL.

2.5. Machine Learning Algorithm for Fatigue Detection

2.5.1. Dataset Preparation

First, to eliminate differences in scale and range among various HRV features, this paper applied min-max normalization to the dataset, converting all features to a range from 0 to 1. Next, a significance analysis was performed on the HRV feature indicators to identify the most relevant physiological indicators. Finally, principal component analysis (PCA) was applied to the selected key features, reducing their dimensionality to suit resource-constrained MCU environments while retaining critical information. The steps of the PCA algorithm are as follows:

1. Form an $N \times M$ matrix $X_{N \times M}$ from the original data after min-max normalization;
2. Perform zero-mean normalization on each row of X (representing a feature), i.e., subtract the mean of each row to obtain the zero-mean matrix A;
3. Compute the covariance matrix $C = \frac{1}{M} A A^T$;
4. Calculate the eigenvalues of C and their corresponding eigenvectors;
5. Arrange the eigenvectors into a matrix in descending order based on their corresponding eigenvalues, and select the top R rows to form the matrix P;
6. $Y = PX$, which represents the data reduced to R-dimensional space.

Principal components with a cumulative variance contribution rate of 95% were retained for model training. Finally, the dataset was randomly divided into training and test sets in a 3:1 ratio.

2.5.2. Classifier Selection and Training

To evaluate the performance of different machine learning approaches in classifying fatigue states, we selected four commonly used algorithms: backpropagation neural network (BPNN), support vector machine (SVM), K-nearest neighbors (KNN), and decision tree (DT). These algorithms were chosen because they are effective in classification tasks and have relatively low computational complexity, making them suitable for deployment in

embedded systems. By comparing these algorithms, we aimed to identify the most efficient and accurate approach for detecting fatigue in resource-constrained environments.

This paper uses the Python Sklearn library to build the aforementioned models. The BPNN model consists of two hidden layers, each with six neurons, and an output layer with one neuron. The SVM model employs a linear kernel function with the gamma parameter set to 2. For the KNN model, the parameter k is set to 19. The DT model is configured with a tree depth of 5, a minimum leaf sample number of 2, and a minimum split sample size of 2. The hyperparameters for each algorithm were selected through preliminary experiments and grid search to achieve the highest classification accuracy on the training dataset. For example, in the case of the KNN algorithm, the number of neighbors (k) was tuned by testing values from 1 to 20 using grid search. The optimal parameter k = 19 was chosen based on the highest accuracy achieved on the training dataset. Model training and testing were conducted on a Windows 10 system equipped with 16 GB of memory and an AMD Ryzen 7 5800 H processor. The detailed steps for implementing the proposed method are outlined in Algorithm 1. Note that the models were trained from scratch without using any pre-trained models.

Algorithm 1: Fatigue Detection Using Machine Learning

Input : Raw HRV dataset X (Raw features: AVNN, SDNN, RMSSD, pNN50, HR, LF, HF, LF/HF, LF (n.u.), HF (n.u.))
Output : Optimal Model C^*

X_norm ← Normalize (X) // Min-max normalization
X_selected ← SignificanceAnalysis (X_norm) // Select key features
X_PCA ← PCA (X_selected, variance = 95%) // PCA retaining 95% variance
TrainSet, TestSet ← Split (X_PCA, ratio = 0.75) // Split dataset
for clf ∈ {BPNN, SVM, KNN, DT} **do**
    Hyperparams ← Tune(clf) // Hyperparameter tuning
    Model ← Train (clf, TrainSet, Hyperparams) // Train classifier
    Accuracy[clf] ← Evaluate (Model, TestSet) // Test classifier
end for
C^* ← argmax(Accuracy) // Select best-performing classifier
Deploy(C^*) // Deploy the selected model

3. Results

3.1. ECG Signal Preprocessing and R-Wave Detection Results

3.1.1. Signal Filtering Results

This paper first applied low-pass filtering to the ECG signal to reduce the powerline interference and EMG noise. Figure 6 shows the changes in the ECG signal sampled at 5 s and 10 s before and after filtering, where the signal becomes smoother and noise is significantly reduced after filtering. The results of frequency spectrum analysis (see Figure 7) indicate that filtering effectively eliminated noise interference above 50 Hz.

In addition, zero-phase filtering was applied to further correct the baseline wander of the signal, as shown in Figure 8. Although zero-phase filtering causes a slight overall delay in the signal, the intervals between R-waves remain unaffected. After filtering, the signal is stable and distortion-free, providing a high-quality data foundation for further analysis.

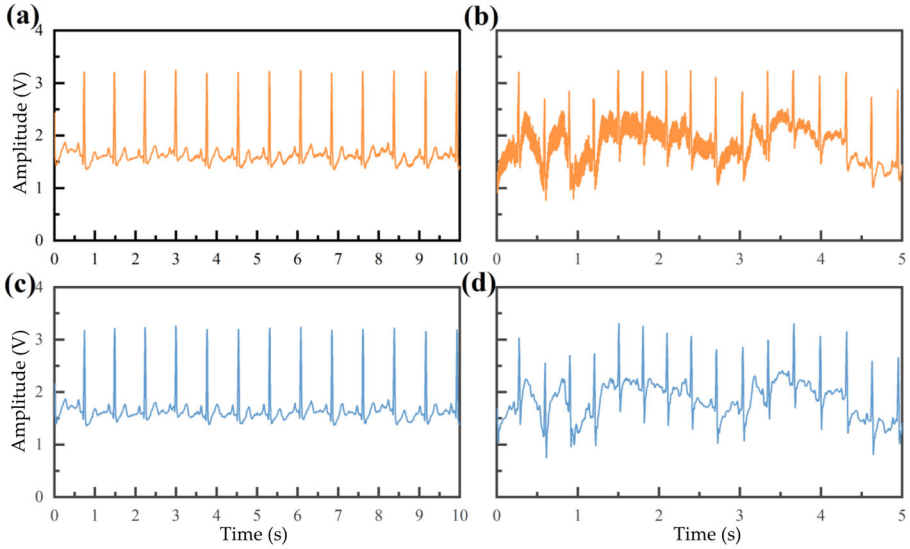


Figure 6. Original and low-pass-filtered ECG signals of 10 s and 5 s. (**a**) Original signal (10 s); (**b**) original signal (5 s); (**c**) signal after low-pass filtering (10 s); (**d**) signal after low-pass filtering (5 s).

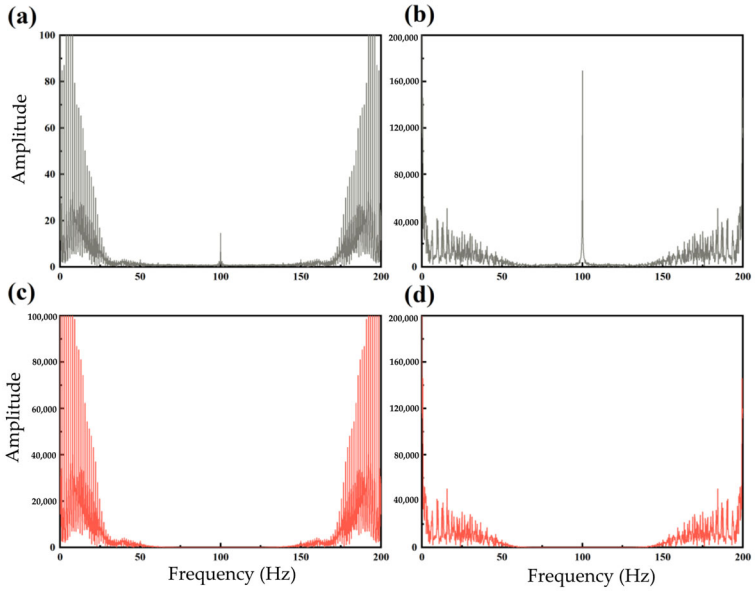


Figure 7. Frequency spectrum of ECG signal before and after low-pass filtering: (**a**) frequency spectrum of original signal (10 s); (**b**) frequency spectrum of original signal (5 s); (**c**) frequency spectrum of filtered signal (10 s); (**d**) frequency spectrum of filtered signal (5 s).

3.1.2. R-Wave Detection Results

Figure 9 shows the R-wave detection results for the ECG signal. The blue dots represent the detected R-wave peaks, while the purple curve is the original signal. The red and green dashed lines indicate the high and low thresholds, respectively. The high threshold is used to identify potential R-wave peaks, while the low threshold helps to distinguish R-waves from noise. The gray dashed line represents the dynamically updated real-time threshold, which is adjusted according to signal fluctuations.

Based on the detected R-wave positions, the RR interval sequence is further calculated. As shown in Figure 10, the time series of the RR intervals uses each RR interval's index as the horizontal axis and the corresponding time value as the vertical axis.

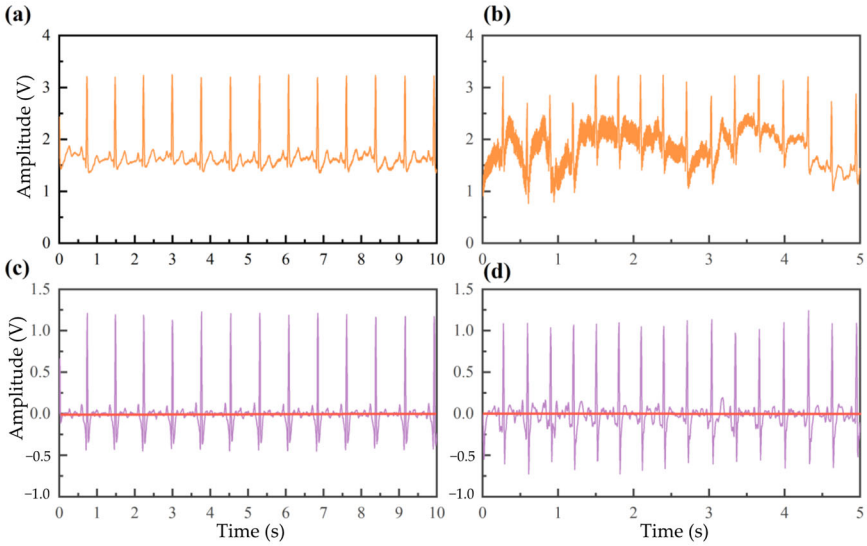


Figure 8. Original and zero-phase filtered signals: (**a**) original signal (10 s); (**b**) original signal (5 s); (**c**) signal after zero-phase filtering (10 s); (**d**) signal after zero-phase filtering (5 s).

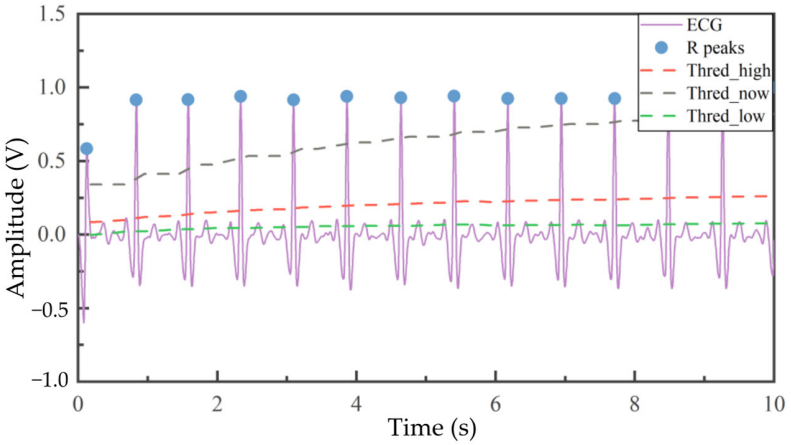


Figure 9. R-wave detection results with dynamic threshold.

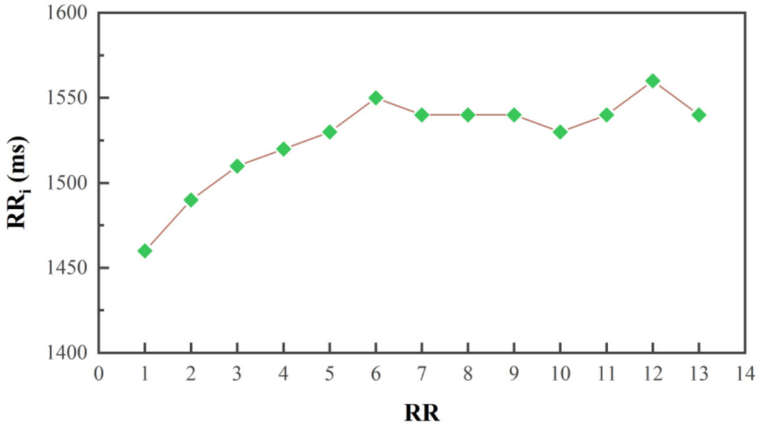


Figure 10. HRV curve based on RR intervals.

3.2. HRV Features Analysis

3.2.1. HRV Features Trend Analysis

In this paper, six segments of ECG signals containing 60,000 sample points were collected from each volunteer during three experimental periods, with a total of 18 volunteers participating in the simulated driving experiment. Therefore, a total of 324 experimental datasets were collected. Additionally, data from other auxiliary experiments were included,

resulting in a total dataset size of 496, with each processed sample containing 10 HRV features. To explore the trend of changes in the HRV features before and after simulated fatigue driving, we conducted statistical analysis on the 496 data and plotted a box plot as shown in Figure 11.

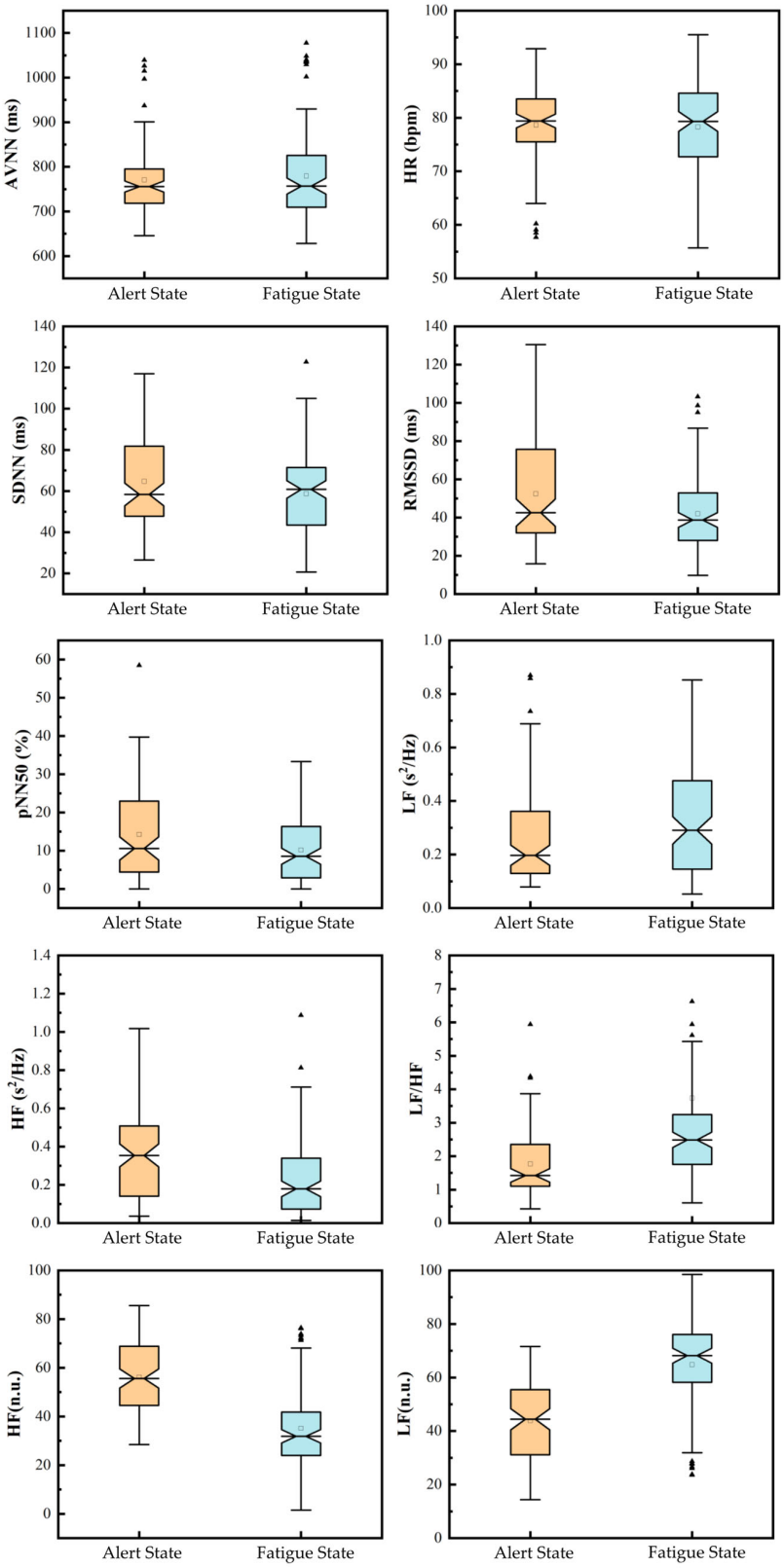


Figure 11. Comparison of HRV features in alert and fatigue states. The dots represent outliers, defined as values beyond 1.5 times the interquartile range (IQR).

Figure 11 shows the trend of the changes in HRV features between alert and fatigue states. Overall, it can be observed that:

1. AVNN and HR: the two are linearly correlated. After driving, the AVNN slightly increases, and the HR slightly decreases. However, due to individual differences, their correlation with the fatigue state is weak;
2. SDNN, RMSSD, and pNN50: these time-domain metrics decrease, indicating a reduction in short-term fluctuations in the RR intervals and a decline in overall HRV variability, reflecting deepening fatigue in the volunteers;
3. LF and LF (n.u.): with the onset of fatigue, LF and its normalized index LF (n.u.) show a significant increase, suggesting that the ANS is attempting to counteract fatigue by enhancing the sympathetic activity;
4. HF and HF (n.u.): high-frequency power HF and its normalized index decrease in the fatigue state, indicating reduced parasympathetic activity and acetylcholine release, which helps maintain a relatively high heart rate;
5. LF/HF: this ratio is significantly elevated in the fatigue state, demonstrating that the sympatho-vagal balance is affected, reflecting rhythm adjustments in the ANS under fatigue.

3.2.2. Significance Analysis of HRV Features

To explore the effectiveness of HRV features in representing the fatigue state, this paper used SPSS 26 for multifactor ANOVA (F-test) and calculated the Pearson correlation coefficients between the features and the fatigue labels (see Table 4). The results indicate that AVNN is significantly correlated with the fatigue state, while SDNN, RMSSD, pNN50, LF/HF, HR, LF (n.u.), and HF (n.u.) are highly significantly correlated, with LF (n.u.) and HF (n.u.) showing the strongest correlation. Among the other features, only LF has a slightly larger F-value. Based on the *p*-value analysis, SDNN, RMSSD, pNN50, and HF (n.u.) are negatively correlated, whereas LF/HF and LF (n.u.) are positively correlated, consistent with the previous analysis.

Table 4. Significance analysis results for HRV features.

HRV Features	F-Value	*p*-Value	Sig-Value
AVNN *	0.410	−0.110	0.014
SDNN **	4.156	−0.127	0.005
RMSSD **	9.216	−0.321	0.000
pNN50 **	7.843	−0.258	0.000
LF	1.175	0.06	0.180
HF	0.276	0.036	0.420
LF/HF **	6.707	0.300	0.000
HR **	0.098	0.138	0.002
LF (n.u.) **	84.376	0.748	0.000
HF (n.u.) **	84.376	−0.748	0.000

*: indicates significance at the 0.05 level; **: indicates significance at the 0.01 level.

Therefore, combining the previous results, further selection for machine learning inputs was conducted among the features SDNN, RMSSD, pNN50, LF, HF, LF/HF, LF (n.u.), and HF (n.u.).

3.3. Gender Differences in HRV

3.3.1. Comparison of HRV Feature Trends

This paper explored the impact of gender on fatigue detection, analyzing the differences in HRV features between males and females in alert and fatigue states. Based on a

sample size of 261 females and 235 males, a box plot comparison analysis of 10 features (see Figure 12) indicates that:

1. AVNN and HR: in the fatigue state, males show higher AVNN values compared to the alert state, while HR exhibits an opposite trend; the difference between the two states is minimal for females;
2. SDNN, RMSSD, and pNN50: in the fatigue state, these three time-domain features for males show a significant decrease, whereas changes in females are more irregular, with some features, such as SDNN and pNN50, even increasing in the fatigue state;
3. LF, LF (n.u.), and LF/HF: these three frequency-domain features increase in both the male and female fatigued groups, with a more pronounced increase in males;
4. HF and HF (n.u.): in the fatigue state, high-frequency features show a decreasing trend in both genders, with a greater decline observed in males.

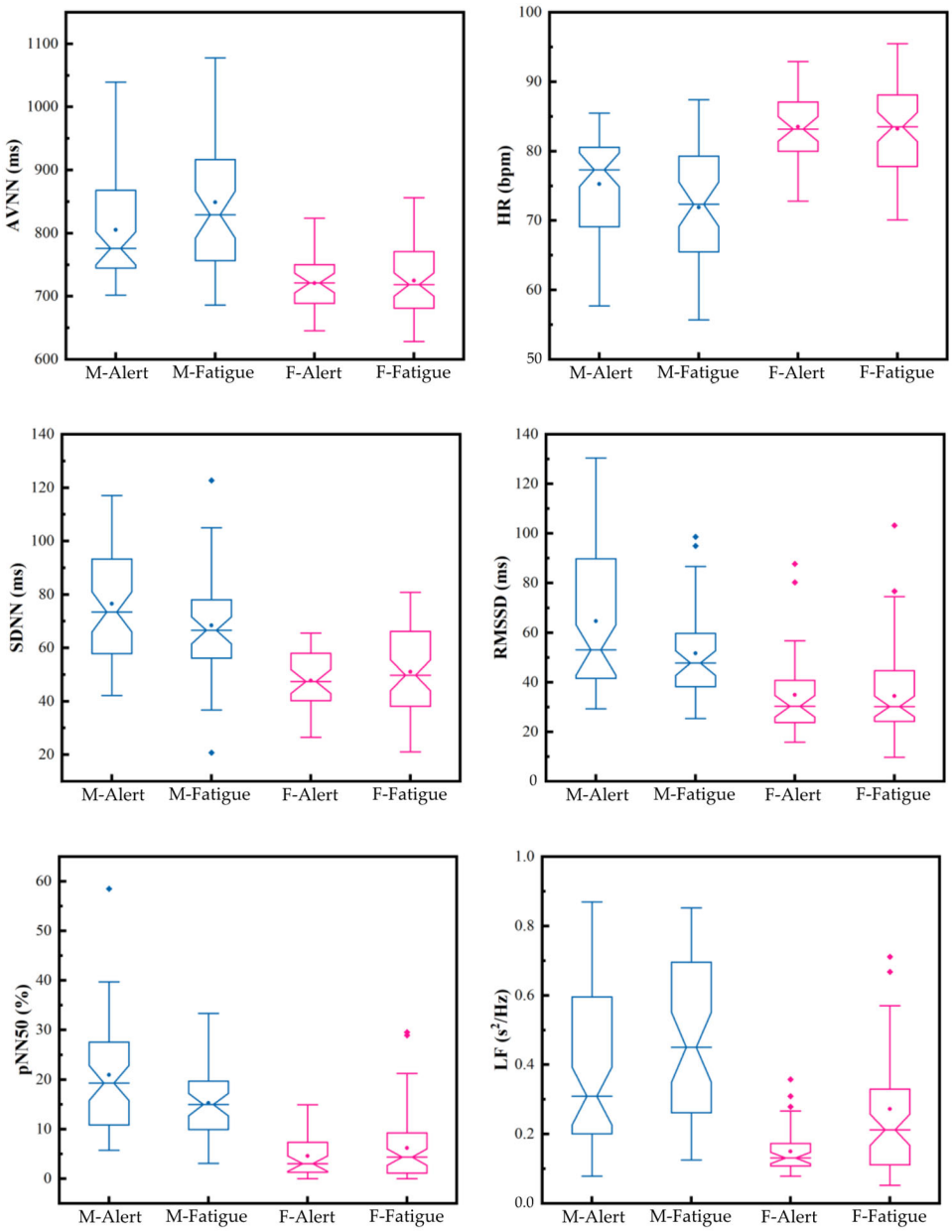


Figure 12. *Cont.*

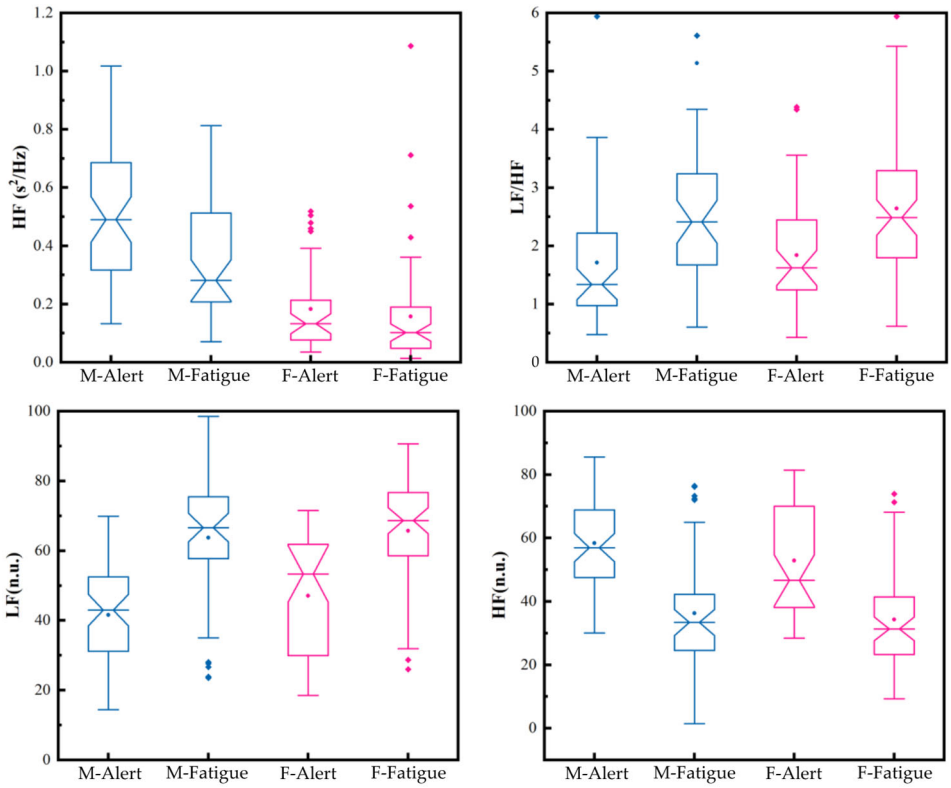


Figure 12. Comparison of HRV features in alert and fatigue states with gender differences. "M" and "F" denote male and female, respectively. The dots represent outliers, defined as values beyond 1.5 times the IQR.

In summary, both time-domain and frequency-domain features reflect gender differences in changing trends under the fatigue state. Males show a stronger and consistent increase in sympathetic activity (LF, LF (n.u.), LF/HF) and a consistent decrease in parasympathetic activity (RMSSD, pNN50, HF, HF (n.u.)), while females exhibit more irregular changes. This demonstrates significant differences in autonomic responses between genders.

3.3.2. Gender Differences in Significance Analysis

To further explore gender differences in HRV features, we conducted a significance analysis of the correlation between the HRV features and the fatigue state for each gender. Table 5 shows that, in the female group, all HRV features except SDNN are significantly correlated with the fatigue state, with LF (n.u.) and HF (n.u.) showing the strongest correlations. In the male group, features such as RMSSD, pNN50, LF/HF, LF (n.u.), and HF (n.u.) are significantly correlated with the fatigue state, with LF (n.u.) and HF (n.u.) exhibiting the strongest correlations as well.

Furthermore, as shown in the table, although LF (n.u.) and HF (n.u.) exhibit the strongest correlations with the fatigue state in both genders, gender-tailored fatigue detection models can achieve better accuracy by focusing on additional features. Specifically, aside from these shared highly correlated features, detection models for females could further emphasize LF and HF, while those for males could be supplement their analysis with SDNN to better capture gender-specific differences and enhance their detection accuracy.

Table 5. Gender-based significance analysis results of HRV features.

HRV Features	Female		Male	
	***p*-Value**	**Sig-Value**	***p*-Value**	**Sig-Value**
AVNN	−0.259 **	0.000	0.009	0.893
SDNN	−0.086	0.165	−0.151 *	0.021
RMSSD	−0.381 **	0.000	−0.303 **	0.000
pNN50	−0.249 **	0.000	−0.289 **	0.000
LF	0.151 *	0.015	0.092	0.161
HF	−0.417 **	0.000	0.058	0.377
LF/HF	0.641 **	0.000	0.272 **	0.000
HR	0.255 **	0.000	0.014	0.836
LF (n.u.)	0.750 **	0.000	0.751 **	0.000
HF (n.u.)	−0.750 **	0.000	−0.751 **	0.000

*: Indicates significance at the 0.05 level; **: indicates significance at the 0.01 level.

3.4. Machine Learning Classifier Evaluation and Deployment

3.4.1. PCA Results

As indicated by the significance analysis in Section 3.2.2, we preliminarily identified that SDNN, RMSSD, pNN50, LF, HF, LF/HF, LF (n.u.), and HF (n.u.) have stronger correlations with fatigue. Therefore, in this section, we used SPSS software to perform PCA on the min-max normalized dataset of these features.

The results show that the first five principal components explain more than 95% of the variance (see Table 6). Therefore, these five components (i.e., SDNN, RMSSD, pNN50, LF, HF) were selected to construct a new dataset for subsequent classifier training.

Table 6. PCA results table.

Number of Components	Initial Eigenvalue		
	Total	**Percentage of Variance**	**Cumulative Percentage**
1	3.829	38.292	38.292
2	2.285	22.847	61.139
3	1.718	17.176	78.315
4	1.033	10.332	88.648
5	0.671	6.713	95.360
6	0.229	2.286	97.646
7	0.171	1.713	99.359
8	0.052	0.520	99.879
9	0.012	0.121	100.000
10	-4.749×10^{-16}	-4.749×10^{-15}	100.000

3.4.2. Evaluation Results of Machine Learning Classifiers

We compared the classification accuracies of four classifiers before and after PCA (see Table 7). The final reported accuracy reflects the model's performance on the reserved test set, which was unseen during the training process. The results show that the BPNN had the most significant improvement in accuracy, while the DT model performed better without PCA. The SVM model showed a slight improvement, and the KNN model's performance remained unchanged.

Additionally, as shown in Figure 13, we plotted the confusion matrices for the four classifiers. Based on the confusion matrices shown, the BPNN performs best in detecting the fatigue state, with minimal misclassifications. The SVM model shows strong accuracy in detecting the alert state but has a relatively high error rate for the fatigue state. The KNN

model achieves the highest accuracy in classifying the alert state, while the DT model's overall performance is comparable to that of the BPNN. Overall, most classifiers tend to classify the alert state as fatigue. However, this conservative strategy helps reduce the risks of fatigue and ensures greater safety. To further evaluate each model's performance, we plotted the ROC curves, as shown in Figure 14. The figure displays the classification effectiveness of each model, with the BPNN achieving the highest AUC value, further demonstrating its optimal classification capability.

Table 7. Comparison of classifier accuracy with and without PCA.

Classifier	Without PCA	With PCA
BPNN	90.31%	94.35%
SVM	89.52%	91.13%
KNN	93.55%	93.55%
DT	93.35%	87.10%

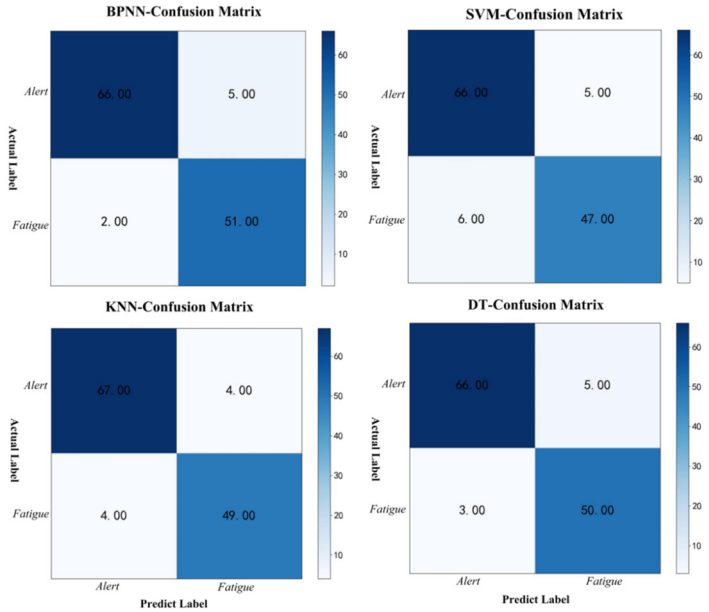


Figure 13. Confusion matrices of the four classifiers.

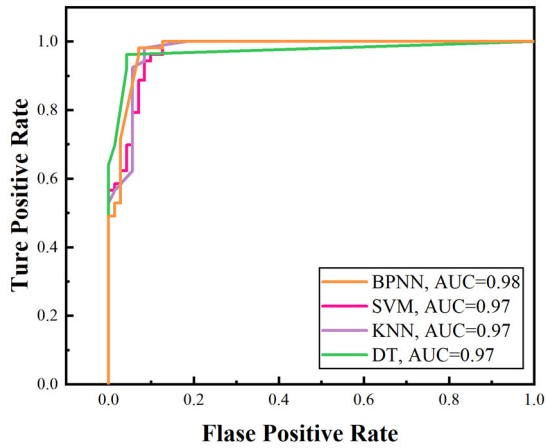


Figure 14. ROC curves of the four classifiers.

In summary, the BPNN is deemed the best classifier in this study, achieving the highest accuracy (94.35%) and AUC value (0.98) among all evaluated classifiers. Although the DT and KNN models show a comparable performance in terms of overall accuracy, the BPNN

demonstrates better consistency. The SVM model, on the other hand, has higher error rates in detecting the fatigue state. Therefore, the BPNN is identified as the most effective and reliable classifier, with the lowest misclassification rate for the fatigue state, which is a critically important metric in practical applications.

3.4.3. Embedded Deployment of the Optimal Model

This paper subsequently selected the BPNN model for embedded deployment, converted it to the ONNX (Open Neural Network Exchange) format, and used STM32CubeMX (version 6.12.0) [59] to generate the initialization code for the STM32F407ZGT6. Due to the limited memory resources of the embedded system, a batch-processing strategy was applied to handle the ECG signal. Specifically, the total of 60,000 data points is divided into 10 batches, with 6000 ECG signals collected and processed in each batch. After each batch is processed, the calculated RR intervals are sequentially stored in an array to ensure the complete recording and processing of all ECG data. Finally, the HRV features extracted from this array are used as inputs to the BPNN.

4. Discussion

The findings suggest that, in fatigue, there is a marked shift in the autonomic balance towards sympathetic dominance, as evidenced by increases in the LF and LF/HF ratios alongside decreases in the HF. This highlights the body's compensatory mechanisms for staying alert when fatigued, but may also indicate a strain on the autonomic system over time. This finding is consistent with existing research and further validates the importance of HRV features as an early indicator of fatigue.

The observed gender differences in HRV feature responses further reveal distinct sensitivities and regulatory mechanisms, which may stem from variations in fatigue and stress management shaped by the physiological structure, hormone levels, and ANS function. These findings highlight the importance of considering gender-specific approaches in broader applications, such as tailoring work schedules or refining traffic safety policies based on individual physiological characteristics.

To comprehensively evaluate the effectiveness of the proposed driver fatigue detection system, we conducted a comparison between our work and recent studies focused on ECG-based methods. The comparison focuses on key aspects such as data types, experiment environments, subject numbers, dataset sizes, detection accuracy, etc. The specific comparison results are summarized in Table 8. The comparison demonstrates that the proposed system achieves competitive accuracy. It outperforms most methods by involving a higher number of participants, while also excelling in portability and cost.

Additionally, the proposed design is significantly more cost-effective and portable than existing commercial fatigue detection systems. For example, systems such as the Volvo Driver Alert Control System (Volvo Car Corporation, Gothenburg, Sweden) [60], Ford Driver Alert System (Ford Motor Company, Dearborn, MI, USA) [61], and Bosch Driver Drowsiness Detection System (Robert Bosch GmbH, Gerlingen, Germany) [62] rely on proprietary hardware and software tightly integrated into vehicles. These systems are typically bundled with advanced trim levels or optional safety packages, resulting in high overall costs and limited adaptability. In contrast, our HRV-based standalone system eliminates the need for vehicle-specific hardware, reducing costs and enabling its use across a wider range of vehicles, including those without built-in detection systems, offering superior portability and adaptability.

Table 8. Comparison of the proposed method with related works.

Ref. and Year	Classification Methods	Data Type/Dataset	Experiment Environment	Number of Subjects	Dataset Size	Gender Difference Analysis	Accuracy (%)	Portability	Cost
Gwak et al., 2020 [8]	Random Forest	EEG, ECG, vehicle data, etc.	simulated driving	16	2847	no	82.4% (slightly drowsy)	low	high
Du et al., 2022 [10]	Product Fuzzy Convolutional Network (PFCN)	EEG, ECG	simulated & real driving	20	N/A	no	94.19	low	high
Zhang et al., 2024 [13]	Random Forest	vehicle data, eye-tracking data, heartbeat intervals, etc.	real driving	18	548,988 data points	no	92.6	low	high
Garcia-Perez et al., 2022 [28]	KNN	HRV (ECG)	simulated driving	12	1080	no	76.5	medium	medium
Halomoan et al., 2023 [29]	Random forest	HRV (ECG)	simulated driving	11	23.59 min/subject	no	86.36	medium	medium
Wang et al., 2023 [30]	statistical methods	HRV (ECG)	simulated driving	16	560 min	no	96.88 (average)	high	medium
Sun et al., 2024 [31]	SVM (RBF kernel)	HRV (ECG)	simulated driving	12	1224	no	87.04	medium	medium
ours	BPNN	HRV (ECG)	simulated driving	18	496 (29,760,000 data points)	yes	94.35	high	low

Finally, this paper also has certain limitations. While the driving simulation dataset used in this study involves a higher number of participants than many existing studies, the total number of participants (18) remains limited, and the dataset mainly consists of young participants. This may constrain our assessment of the model's generalization capabilities across more diverse populations. Despite this, we have ensured the robustness of the results through cross-validation to minimize the risk of overfitting and bias. Therefore, the current study provides a promising model with good performance on the available dataset and potential applicability to broader contexts. We plan to further enhance the model's generalization capabilities by training it on a larger and more diverse dataset, including participants across a broader age range and varying demographics. Additionally, we will continue to investigate the effects of gender and age differences across different groups and aim to validate the system's performance under real-world driving conditions.

5. Conclusions

Fatigue is a leading cause of traffic accidents, and its early detection is therefore crucial for timely intervention and improved road safety. To address this issue, this study proposes a cost-effective and wearable system for early driver fatigue detection. The system consists of several key modules, including wearable ECG signal acquisition, HRV feature extraction, a machine learning-based fatigue classifier, and embedded deployment. ECG signals are captured using wired wearable devices, preprocessed to extract HRV features, and analyzed using a machine learning model optimized for embedded systems. Additionally, this study investigates gender differences in HRV features during fatigue states, laying the foundation for the development of gender-tailored fatigue detection models that have improved accuracy and adaptability in practical applications. Experiments in a simulated driving environment were used to evaluate the system's performance across multiple machine learning models and configurations, with the optimized BPNN achieving the highest detection accuracy of 94.35%. Unlike existing commercial systems that rely on proprietary hardware, the proposed system is cost-effective, portable, and adaptable to various vehicles. It is suitable for real-world applications, especially in vehicles without built-in detection systems, and its ability to provide early fatigue warnings makes it a practical solution to improve road safety and reduce fatigue-related accidents. Due to the requirements for data acquisition accuracy, this study uses wired connection devices. However, as flexible wireless ECG sensing technology continues to mature, the approach presented in this study remains a valid technical route. In the future, the system's portability and usability can be further improved by integrating non-intrusive wireless wearable devices. Another important area of study that can be explored in the future is the acquisition of additional physiological signals such as eye movement and EEG, as well as data from more diverse driving environments, to enhance the robustness and predictive accuracy of the model.

Author Contributions: Conceptualization, C.L., X.Z. and Y.X.; methodology, C.L. and X.Z.; software, X.Z. and R.W.; validation, C.L., X.Z. and R.W.; formal analysis, C.L., X.Z. and R.W.; investigation, C.L. and X.Z.; resources, C.L.; data curation, C.L.; writing—original draft preparation, C.L. and X.Z.; writing—review and editing, C.L., X.Z, R.W., W.Z., N.L. and Y.X.; visualization, C.L., X.Z. and R.W.; supervision, W.Z., N.L. and Y.X.; project administration, Y.X. All authors have read and agreed to the published version of the manuscript.

Funding: This research received no external funding.

Data Availability Statement: The data presented in this study are available on request from the corresponding author due to privacy restrictions.

Acknowledgments: The authors would like to express sincere gratitude to all the participants who volunteered their time and effort in this study.

Conflicts of Interest: The authors declare no conflicts of interest.

References

1. Study: Fatalities Due to Drowsiness 10× Higher Than Reported. Available online: https://newsroom.acg.aaa.com/study-fatalities-due-to-drowsiness-10x-higher-than-reported (accessed on 18 December 2024).
2. Measures for the Administration of Penalty Points for Road Traffic Safety Offenses. Available online: https://www.gov.cn/gongbao/content/2022/content_5679697.html (accessed on 4 November 2024).
3. Regulation (EC) No 561/2006 of the European Parliament and of the Council. Available online: https://eur-lex.europa.eu/legal-content/EN/TXT/?uri=CELEX:32006R0561 (accessed on 4 November 2024).
4. Summary of Hours of Service Regulations. Available online: https://www.fmcsa.dot.gov/regulations/hours-service/summary-hours-service-regulations (accessed on 4 November 2024).
5. Fu, S.; Yang, Z.; Ma, Y.; Li, Z.; Xu, L.; Zhou, H. Advancements in the intelligent detection of driver fatigue and distraction: A comprehensive review. *Appl. Sci.* **2024**, *14*, 3016. [CrossRef]
6. El-Nabi, S.A.; El-Shafai, W.; El-Rabaie, E.S.M.; Ramadan, K.F.; Abd El-Samie, F.E.; Mohsen, S. Machine learning and deep learning techniques for driver fatigue and drowsiness detection: A review. *Multimed. Tools Appl.* **2024**, *83*, 9441–9477. [CrossRef]
7. Fu, B.; Boutros, F.; Lin, C.T.; Damer, N. A survey on drowsiness detection—Modern applications and methods. *IEEE Trans. Intell. Veh.* 2024; *Early Access*.
8. Gwak, J.; Hirao, A.; Shino, M. An Investigation of Early Detection of Driver Drowsiness Using Ensemble Machine Learning Based on Hybrid Sensing. *Appl. Sci.* **2020**, *10*, 2890. [CrossRef]
9. Zhao, L.; Li, M.; He, Z.; Ye, S.; Qin, H.; Zhu, X.; Dai, Z. Data-driven learning fatigue detection system: A multimodal fusion approach of ECG (electrocardiogram) and video signals. *Measurement* **2022**, *201*, 111648. [CrossRef]
10. Du, G.; Long, S.; Li, C.; Wang, Z.; Liu, P.X. A product fuzzy convolutional network for detecting driving fatigue. *IEEE Trans. Cybern.* **2022**, *53*, 4175–4188. [CrossRef] [PubMed]
11. Shi, J.; Wang, K. Fatigue driving detection method based on time-space-frequency features of multimodal signals. *Biomed. Signal Process. Control* **2023**, *84*, 104744. [CrossRef]
12. He, C.; Xu, P.; Pei, X.; Wang, Q.; Yue, Y.; Han, C. Fatigue at the wheel: A non-visual approach to truck driver fatigue detection by multi-feature fusion. *Accid. Anal. Prev.* **2024**, *199*, 107511. [CrossRef]
13. Zhang, N.; Zhang, Z.; Ma, C.; Yang, Z.; Zhang, S.; Wu, J. Fatigue driving state detection for tanker truck drivers based on multi-feature fusion. In Proceedings of the Fourth International Conference on Smart City Engineering and Public Transportation, Beijing, China, 26–28 January 2024; Volume 13160, pp. 225–232.
14. Ansari, S.; Du, H.; Naghdy, F.; Stirling, D. Automatic driver cognitive fatigue detection based on upper body posture variations. *Expert Syst. Appl.* **2022**, *203*, 117568. [CrossRef]
15. Zhu, T.; Zhang, C.; Wu, T.; Ouyang, Z.; Li, H.; Na, X.; Liang, J.; Li, W. Research on a Real-Time Driver Fatigue Detection Algorithm Based on Facial Video Sequences. *Appl. Sci.* **2022**, *12*, 2224. [CrossRef]
16. Lu, Y.; Liu, C.; Chang, F.; Liu, H.; Huan, H. JHPFA-Net: Joint head pose and facial action network for driver yawning detection across arbitrary poses in videos. *IEEE Trans. Intell. Transp. Syst.* **2023**, *24*, 11850–11863. [CrossRef]
17. Yi, Y.; Zhang, H.; Zhang, W.; Yuan, Y.; Li, C. Fatigue working detection based on facial multifeature fusion. *IEEE Sens. J.* **2023**, *23*, 5956–5961. [CrossRef]
18. Li, X.; Lin, H.; Du, J.; Yang, Y. Computer vision-based driver fatigue detection framework with personalization threshold and multi-feature fusion. *Signal Image Video Process.* **2024**, *18*, 505–514. [CrossRef]
19. Davanathan, S.; Taujuddin, N.S.A.M.; Sari, S. Driving fatigue detection system using Haar cascade technique. *Evol. Electr. Electron. Eng.* **2024**, *5*, 436–442.
20. Demestichas, K.; Alexakis, T.; Peppes, N.; Adamopoulou, E. Comparative analysis of machine learning-based approaches for anomaly detection in vehicular data. *Vehicles* **2021**, *3*, 171–186. [CrossRef]
21. Guo, H.; Weng, J.; Lin, C. An adaptive fatigue driving detection method based on BP-SVM. In Proceedings of the International Conference of Transportation Professionals (CICTP 2023), Beijing, China, 14–17 July 2023; pp. 1246–1255.
22. Harvy, J.; Bezerianos, A.; Li, J. Reliability of EEG measures in driving fatigue. *IEEE Trans. Neural Syst. Rehabil. Eng.* **2022**, *30*, 2743–2753. [CrossRef] [PubMed]
23. Subasi, A.; Saikia, A.; Bagedo, K.; Singh, A.; Hazarika, A. EEG-based driver fatigue detection using FAWT and multiboosting approaches. *IEEE Trans. Ind. Inf.* **2022**, *18*, 6602–6609. [CrossRef]
24. Chen, C.; Ji, Z.; Sun, Y.; Bezerianos, A.; Thakor, N.; Wang, H. Self-attentive channel-connectivity capsule network for EEG-based driving fatigue detection. *IEEE Trans. Neural Syst. Rehabil. Eng.* **2023**, *31*, 3152–3162. [CrossRef] [PubMed]
25. Li, Q.; Luo, Z.; Qi, R.; Zheng, J. Automatic searching of lightweight and high-performing CNN architectures for EEG-based driving fatigue detection. *IEEE Trans. Instrum. Meas.* **2024**, *73*, 1–11. [CrossRef]

26. Hu, F.; Zhang, L.; Yang, X.; Zhang, W.A. EEG-based driver fatigue detection using spatio-temporal fusion network with brain region partitioning strategy. *IEEE Trans. Intell. Transp. Syst.* **2024**, *25*, 9618–9630. [CrossRef]
27. Zhao, P.; Lian, C.; Xu, B.; Zeng, Z. Multiscale global prompt transformer for EEG-based driver fatigue recognition. *IEEE Trans. Autom. Sci. Eng.* 2024; *Early Access*.
28. Garcia-Perez, S.; Rodríguez, M.D.; Lopez-Nava, I.H. Towards recognition of driver drowsiness states by using ECG signals. In Proceedings of the International Conference on Ubiquitous Computing and Ambient Intelligence, Córdoba, Spain, 29 November–2 December 2022; pp. 369–380.
29. Halomoan, J.; Ramli, K.; Sudiana, D.; Gunawan, T.S.; Salman, M. A New ECG Data Processing Approach to Developing an Accurate Driving Fatigue Detection Framework with Heart Rate Variability Analysis and Ensemble Learning. *Information* **2023**, *14*, 210. [CrossRef]
30. Wang, F.; Yao, W.; Lu, B.; Fu, R. ECG-based real-time drivers' fatigue detection using a novel elastic dry electrode. *IEEE Trans. Instrum. Meas.* **2024**, *73*, 1–16. [CrossRef]
31. Sun, W.; Jiang, W.; Li, C.; Si, Y.; Li, S.; Guo, M.; Song, H. Study on identification method of driver fatigue considering individual ECG differences. *Cogn. Technol. Work* **2024**, *26*, 301–312. [CrossRef]
32. Mahmood, H.R.; Irshayyid, M.S.; Hussien, M.K. Measuring the fatigue of persons based on EOG signal processing methods. In Proceedings of the International Conference on Engineering Technology and Its Applications, Al-Najaf, Iraq, 31 May–1 June 2022; pp. 283–288.
33. Murugan, S.; Sivakumar, P.K.; Kavitha, C.; Harichandran, A.; Lai, W.-C. An Electro-Oculogram (EOG) Sensor's Ability to Detect Driver Hypovigilance Using Machine Learning. *Sensors* **2023**, *23*, 2944. [CrossRef] [PubMed]
34. Das, A.K.; Kumar, P.; Halder, S.; Metia, S. A statistical approach for investigation and comparison of fatigue and drowsiness based on complexity parameters of EOGs. *Int. J. Image Graph. Signal Process.* **2023**, *15*, 39–59.
35. Das, A.K.; Kumar, P.; Halder, S. Complexity analysis of ocular signal for detection of human fatigue using small datasets. *Procedia Comput. Sci.* **2023**, *218*, 858–866. [CrossRef]
36. Rahman, N.A.; Mustafa, M.; Sulaiman, N.; Samad, R.; Abdullah, N.R.H. EMG signal segmentation to predict driver's vigilance state. In Proceedings of the Human Engineering Symposium, Pekan, Pahang, Malaysia, August 2020; pp. 29–42.
37. Mohanavelu, K.; Lamshe, R.; Poonguzhali, S.; Adalarasu, K.; Jagannath, M. Assessment of human fatigue during physical performance using physiological signals: A review. *Biomed. Pharmacol. J.* **2017**, *10*, 1887–1896. [CrossRef]
38. Niermann, D.; Trende, A.; Ihme, K.; Drewitz, U.; Hollander, C.; Hartwich, F. An integrated model for user state detection of subjective discomfort in autonomous vehicles. *Vehicles* **2021**, *3*, 764–777. [CrossRef]
39. Freitas, A.; Almeida, R.; Gonçalves, H.; Conceição, G.; Freitas, A. Monitoring fatigue and drowsiness in motor vehicle occupants using electrocardiogram and heart rate: A systematic review. *Transp. Res. Part F Traffic Psychol. Behav.* **2024**, *103*, 586–607. [CrossRef]
40. Apparies, R.J.; Riniolo, T.C.; Porges, S.W. A psychophysiological investigation of the effects of driving longer-combination vehicles. *Ergonomics* **1998**, *41*, 581–592. [CrossRef]
41. Shaffer, F.; Ginsberg, J.P. An overview of heart rate variability metrics and norms. *Front. Public Health* **2017**, *5*, 258. [CrossRef]
42. Everything You Need to Know About Heart Rate Variability (HRV). Available online: https://www.whoop.com/us/en/thelocker/heart-rate-variability-hrv/ (accessed on 4 November 2024).
43. How To Improve Your HRV (Heart Rate Variability). Available online: https://ouraring.com/blog/improve-hrv/ (accessed on 4 November 2024).
44. Understanding HRV Status on Your Garmin Device. Available online: https://www.garmin.com.sg/minisite/garmin-technology/health-science/hrv-status/ (accessed on 4 November 2024).
45. Fitbit Community. Available online: https://community.fitbit.com/t5/Community/ct-p/EN (accessed on 4 November 2024).
46. Monitor Heart Rate with Apple Watch. Available online: https://support.apple.com/en-us/120277 (accessed on 4 November 2024).
47. Warden, P.; Situnayake, D. *TinyML: Machine Learning with TensorFlow Lite on Arduino and Ultra-Low-Power Microcontrollers*; O'Reilly Media: Sebastopol, CA, USA, 2019; p. 3.
48. Pomoni, M. Exploring smart tires as a tool to assist safe driving and monitor tire–road friction. *Vehicles* **2022**, *4*, 744–765. [CrossRef]
49. Reddy, B.; Kim, Y.H.; Yun, S.; Seo, C.; Jang, J. Real-time driver drowsiness detection for embedded system using model compression of deep neural networks. In Proceedings of the IEEE Conference on Computer Vision and Pattern Recognition Workshops, Honolulu, HI, USA, 21–26 July 2017; pp. 121–128.
50. Sahin, M.E. Real-time driver drowsiness detection and classification on embedded systems using machine learning algorithms. *Trait. Signal* **2023**, *40*, 847. [CrossRef]
51. Abirami, A.; Bhuvaneswari, S.; Vishnuvardhan, M.; Karthik, Y.; Shankar, S. An in-depth exploration of advanced driver drowsiness detection systems for enhanced road safety. In Proceedings of the International Conference on Computer, Communication and Control, Indore, India, 8–10 February 2024; pp. 1–6.

52. Peng, Z.; Wang, G. A novel ECG eigenvalue detection algorithm based on wavelet transform. *Biomed. Res. Int.* **2017**, *2017*, 5168346. [CrossRef] [PubMed]
53. Kher, R. Signal processing techniques for removing noise from ECG signals. *J. Biomed. Eng. Res.* **2019**, *3*, 1–9.
54. Pan, J.; Tompkins, W.J. A real-time QRS detection algorithm. *IEEE Trans. Biomed. Eng.* **1985**, *3*, 230–236. [CrossRef] [PubMed]
55. Welch, P. The use of fast Fourier transform for the estimation of power spectra: A method based on time averaging over short, modified periodograms. *IEEE Trans. Audio Electroacoust.* **1967**, *15*, 70–73. [CrossRef]
56. Åkerstedt, T.; Gillberg, M. Subjective and objective sleepiness in the active individual. *Int. J. Neurosci.* **1990**, *52*, 29–37. [CrossRef] [PubMed]
57. Deng, Z.; Gao, Y.; Li, T. Comparison on driving fatigue related hemodynamics activated by auditory and visual stimulus. In Proceedings of the Clinical and Translational Neurophotonics, San Francisco, CA, USA, 27–28 January 2018; Volume 10480, pp. 56–61.
58. Mueller, S.T.; Piper, B.J. The psychology experiment building language (PEBL) and PEBL test battery. *J. Neurosci. Methods* **2014**, *222*, 250–259. [CrossRef] [PubMed]
59. STM32Cube Initialization Code Generator. Available online: https://www.st.com/en/development-tools/stm32cubemx.html (accessed on 7 November 2024).
60. How Driver Alert Control Works. Available online: https://www.crestvolvocars.com/blog/2017/march/28/how-driver-alert-control-works.htm (accessed on 27 December 2024).
61. How do I use the Driver Alert System * in my Ford? Available online: https://www.ford.com/support/how-tos/ford-technology/driver-assist-features/how-do-i-use-the-driver-alert-system/ (accessed on 27 December 2024).
62. Driver Drowsiness Detection. Available online: https://www.bosch-mobility.com/en/solutions/assistance-systems/driver-drowsiness-detection/ (accessed on 27 December 2024).

Disclaimer/Publisher's Note: The statements, opinions and data contained in all publications are solely those of the individual author(s) and contributor(s) and not of MDPI and/or the editor(s). MDPI and/or the editor(s) disclaim responsibility for any injury to people or property resulting from any ideas, methods, instructions or products referred to in the content.